Vietnam Journal of Mechanics, Vietnam Academy of Science and Technology
DOI: https://doi.org/10.15625/0866-7136/23571

FINITE ELEMENT ANALYSIS OF GUIDED WAVE DISPERSION IN PIPES WITH MULTICHANNEL ACQUISITION

Ductho Le[1], **Hoang Ngoc Quy**[2,3], **Haidang Phan**[3], **Hoai Nguyen**[4,*]
[1]*Department of Radiology and Diagnostic Imaging, University of Alberta, Edmonton, Alberta, Canada*
[2]*Institute of Mechanics, Vietnam Academy of Science and Technology, Hanoi, Vietnam*
[3]*Faculty of Civil Engineering, VNU University of Engineering and Technology, Hanoi, Vietnam*
[4]*Institute of Physics, Vietnam Academy of Science and Technology, Hanoi, Vietnam*
[*]E-mail: hoai.ngo@gmail.com

Received: 02 October 2025 / Revised: 03 November 2025 / Accepted: 22 November 2025
Published online: 15 December 2025

Abstract. Ultrasonic guided waves have become a key tool in nondestructive evaluation of pipelines, as they can travel long distances with low attenuation while maintaining high sensitivity to defects. Accurate modeling of their dispersion characteristics is essential for inspection design and signal interpretation. This study presents a finite element (FE) framework that advances beyond conventional eigenvalue-based analyses by directly simulating a realistic multichannel acquisition process. A pitch-catch configuration, consisting of a ring actuator and a linear receiver array, is modeled, and dispersion spectra are reconstructed through two-dimensional Fourier transforms—closely mirroring experimental practice. The reconstructed spectra show excellent agreement with analytical solutions, thereby validating the approach. By bridging numerical modeling and experimental acquisition, this FE framework delivers realistic datasets that facilitate advanced signal processing, imaging algorithms, and pipeline inspection strategies.

Keywords: ultrasonic guided waves, dispersion curves, finite element analysis, multichannel acquisition, pipeline inspection, nondestructive evaluation.

1. INTRODUCTION

Pipelines are critical infrastructures for transporting energy, chemicals, and water, and their safe operation is essential for protecting the environment and society. Failures due to corrosion, fatigue, or weld defects can cause catastrophic consequences, including environmental damage, economic loss, and safety hazards. To mitigate such risks, nondestructive evaluation (NDE) techniques are employed to monitor pipeline integrity without service interruption. Among these, ultrasonic guided waves (UGWs) are attractive because they can propagate over long distances with low attenuation while remaining highly sensitive to diverse defects (Sarwar et al., 2024; Zang et al., 2023).

Unlike bulk waves, UGWs are bounded by structural geometry and support multiple mode families in cylindrical waveguides, including longitudinal (L), torsional (T), and flexural (F) modes (Rose, 2014). Each mode exhibits distinct displacement patterns and defect interactions. Dispersion, where phase and group velocities depend on frequency, distorts waveforms but also enables mode selection to optimize defect detection and inspection coverage (Huthwaite et al., 2013; Lowe et al., 2015). Foundational work by Chree (1889) and Pochhammer (1876), later advanced by Cooper and Naghdi (1957), Gazis (1959), Ghosh (1923), Qu and Jacobs (2003), and Sun et al. (2005), established the theoretical basis of guided waves in isotropic cylinders.

However, analytical solutions are limited to idealized, homogeneous, and infinite geometries, whereas real pipelines may include coatings, multilayers, anisotropy, fluid loading, and welds.

To address these complexities, both semi-analytical and numerical approaches have been developed. Notable examples include the semi-analytical finite element method (Cong et al., 2017; Hayashi et al., 2003), the spectral collocation method (Adamou & Craster, 2004; Kiefer, 2024; Le, Phan, et al., 2025), and the Legendre polynomial approach (Jie et al., 2021; Zhang et al., 2021). These methods, however, do not readily replicate experimental measurements. In contrast, the finite element method (FEM) offers a more general framework, capable of accommodating arbitrary geometries, material heterogeneity, and complex boundary conditions. FEM has been applied to a broad range of guided wave problems in pipelines, including dispersion analysis (Sorohan et al., 2011), scattering phenomena (Le, Tran, et al., 2025; Maruyama et al., 2025; Nasedkina et al., 2016), pipe bends (Demma et al., 2005), multilayered configurations (Predoi, 2014), and fluid-filled pipes (Maess et al., 2007). Nevertheless, most FEM-based dispersion studies remain eigenvalue-focused, producing idealized frequency–wavenumber relationships rather than reproducing the type of data acquired in experimental inspections.

In practice, inspections rely on phased arrays and multichannel systems. Phased arrays enable beam steering and focusing, while multichannel receivers provide the time–space datasets essential for advanced techniques such as full matrix capture and the total focusing method (Holmes et al., 2005, 2008). These datasets are typically analyzed with two-dimensional Fourier transforms to obtain dispersion spectra. In this study, the acquisition process is replicated numerically using FEM: guided waves are excited by a phased array actuator and recorded by a linear multichannel receiver array in COMSOL Multiphysics. Fourier analysis of the simulated time–space data produces dispersion spectra that not only mirror experimental practice but also show excellent agreement with analytical solutions when sufficient mesh resolution is used. This FEM–acquisition framework provides realistic datasets for signal processing, array design, and inspection strategy development, and is readily extensible to multilayered or anisotropic pipes, fluid–structure interactions, and defect scattering—thereby bridging numerical modeling and experimental practice.

2. METHODOLOGY

This section presents the FE framework for modeling guided-wave propagation in pipes. The formulation begins with the governing elastodynamic equations and their weak form, followed by FE discretization, time integration, and absorbing boundaries. Phased-array excitation is introduced as surface traction loads with controllable delays, while multichannel acquisition is implemented by recording responses at discrete receiver positions. Finally, dispersion spectra are reconstructed from the simulated datasets using two-dimensional Fourier transforms.

2.1. Finite element formulation

Consider a linear elastic pipe occupying domain Ω with boundary Γ. The displacement vector is denoted by $\mathbf{u}(\mathbf{x}, t)$, the mass density by ρ, and the infinitesimal strain tensor by $\boldsymbol{\varepsilon} = \left(\nabla\mathbf{u} + \nabla\mathbf{u}^T\right)/2$. The corresponding stress tensor is given by $\boldsymbol{\sigma} = \mathbf{C}\colon \boldsymbol{\varepsilon}$, where $\mathbf{C}$ is the fourth-order stiffness tensor. The elastodynamic balance of linear momentum is

$$\nabla \cdot \boldsymbol{\sigma} + \mathbf{b} = \rho\ddot{\mathbf{u}}, \tag{1}$$

where, $\mathbf{b}$ denotes a body force, typically neglected for surface-mounted excitation. For isotropy, $\mathbf{C}$ is determined by Lamé parameters λ, μ or compressional and shear wave speeds $\left(c_p = \sqrt{(\lambda + 2\mu)/\rho}, c_s = \sqrt{\mu/\rho}\right)$.

Boundary conditions are prescribed on displacement and traction subsets of Γ, i.e.,

$$\mathbf{u} = \bar{\mathbf{u}} \text{ on } \Gamma_u, \quad \boldsymbol{\sigma} \cdot \mathbf{n} = \bar{\mathbf{t}} \text{ on } \Gamma_t, \tag{2}$$

where $\mathbf{n}$ is the unit outward normal.

Applying the Galerkin procedure to Eq. (1), the equilibrium equation is multiplied by an admissible virtual displacement field $\delta\mathbf{u}$ and integrated over the domain. By using the divergence theorem, the stress term is transformed into a boundary integral that naturally incorporates the displacement and traction boundary conditions defined in Eq. (2). This yields the weak form as

$$\int_{\Omega} \rho\delta\mathbf{u}\cdot\ddot{\mathbf{u}}\,\mathrm{d}\Omega + \int_{\Omega} \boldsymbol{\varepsilon}\left(\delta\mathbf{u}\right) : \mathbf{C} : \boldsymbol{\varepsilon}\left(\mathbf{u}\right)\,\mathrm{d}\Omega = \int_{\Gamma_t} \delta\mathbf{u}\cdot\bar{\mathbf{t}}\,\mathrm{d}\Gamma. \tag{3}$$

It should be noted that the surface-mounted actuators contribute through the boundary integral on Γ_t, while body forces are neglected.

The displacement field is approximated by shape functions $\mathbf{N}$ with nodal degrees of freedom $\mathbf{d}(t)$, i.e., $\mathbf{u} \approx \mathbf{N}\mathbf{d}$. The strain–displacement matrix $\mathbf{B}$ satisfies $\boldsymbol{\varepsilon} \approx \mathbf{B}\mathbf{d}$. Substituting into Eq. (3), assembling over elements, and collecting terms gives the semi-discrete system, see Rose (2014),

$$\mathbf{M}\ddot{\mathbf{d}} + \mathbf{K}\mathbf{d} = \mathbf{f}\left(t\right), \tag{4}$$

with mass, stiffness, and external force matrices defined as

$$\mathbf{M} = \int_{\Omega} \rho\mathbf{N}^T\mathbf{N}\,\mathrm{d}\Omega, \quad \mathbf{K} = \int_{\Omega} \mathbf{B}^T\mathbf{C}\mathbf{B}\,\mathrm{d}\Omega, \quad \mathbf{f} = \int_{\Gamma_t} \mathbf{N}^T\bar{\mathbf{t}}\mathrm{d}\Gamma. \tag{5}$$

To minimize phase error, the mesh density is selected such that each bulk wavelength is resolved by at least 10–12 nodes. Across the pipe wall, 2–3 quadratic or 4–6 linear elements are used to capture mode shapes near cut-on. Along the pipe axis, element size is constrained by the smallest guided-wave wavelength in the targeted frequency band.

Time integration of Eq. (4) is performed using the implicit Newmark–β method with average acceleration ($\beta = 1/4, \gamma = 1/2$), ensuring unconditional stability. Because the computational model represents a finite pipe length, artificial reflections at the ends must be suppressed. Perfectly matched layers (PML) are employed for this purpose. When the PML thickness and grading are properly tuned, both the frequency-domain complex stretching and its time-domain counterpart can effectively suppress spurious reflections.

2.2. Phased array excitation

Surface-bonded actuators are modeled as traction loads applied on a boundary subset Γ_a. The traction is expressed as

$$\bar{\mathbf{t}}\left(\mathbf{x}, t\right) = \mathbf{q}\left(\mathbf{x}\right) s\left(t\right), \quad \mathbf{x} \in \Gamma_a, \tag{6}$$

where $\mathbf{q}(\mathbf{x})$ defines the loading direction (radial or axial for longitudinal $L(0,m)$ modes, circumferential for torsional $T(0,m)$ modes) and $s\left(t\right)$ is a temporal pulse, which may take the form of a windowed sinusoidal burst or a band-limited wavelet centered at frequency f_0. The elemental nodal load vector is then

$$\mathbf{f}^e\left(t\right) = \int_{\Gamma_a^e} \mathbf{N}^T\mathbf{q}\left(\mathbf{x}\right) s\left(t\right)\mathrm{d}\Gamma, \tag{7}$$

which introduces the excitation into the FE system as a surface traction.

For an array of M actuator elements positioned at axial coordinates z_m (or circumferential angles θ_m), the excitation at each element can include an amplitude weight a_m and a delay τ_m, i.e.,

$$s_m\left(t\right) = a_m s\left(t - \tau_m\right). \tag{8}$$

The choice of delay law governs the effective wavefront generated in the waveguide. In bulk phased arrays, beam steering usually refers to rotating the angle of incidence in a homogeneous medium. In contrast, in pipes, the geometry constrains waves to propagate along the guide, and "steering" is understood as selecting a targeted wave mode.

2.3. Multichannel acquisition

To replicate experimental inspections, responses are acquired not at a single point but across a sequence of receivers distributed along the pipe wall. In the finite element model, these receivers are represented by nodal points positioned at z_j with uniform spacing Δz, such that

$$z_j = z_0 + (j-1)\,\Delta z, \quad j = 1, \ldots, N_z. \tag{9}$$

At each receiver, the displacement or velocity time history is recorded over a simulation window T, discretized into N_t samples with time step Δt

$$U\left(z_j, t_l\right), \quad t_l = (l-1)\,\Delta t, \quad l = 1, \ldots, N_t. \tag{10}$$

Stacking these recordings produces a two-dimensional dataset,

$$\mathbf{U} = \left\{U\left(z_j, t_l\right)\right\} \in \mathbb{R}^{N_z \times N_t}, \tag{11}$$

which directly parallels experimental multichannel acquisition. Each row corresponds to a receiver channel, while each column represents a snapshot of the propagating field at a given time.

Accurate dispersion extraction requires careful design of the sampling parameters. The temporal sampling step Δt must be small enough to capture the highest frequency of interest, and the total recording duration $T = N_t \Delta t$ must be long enough to resolve narrow spectral peaks. The aperture length $A_z = (N_z - 1)\,\Delta z$ strongly influences wavenumber resolution: a longer aperture narrows the main lobe in the spectral domain, enabling separation of closely spaced modes. These considerations ensure that the simulated dataset not only reproduces the wave physics but also reflects the sampling constraints of experimental systems.

2.4. Dispersion extraction via 2D FFT

The dataset $\mathbf{U}(z,t)$ contains guided waves as a superposition of modes, each characterized by distinct frequency–wavenumber pairs. To reconstruct dispersion spectra, a two-dimensional discrete Fourier transform is applied

$$\tilde{U}\left(k, \omega\right) = \sum_{j=1}^{N_z} \sum_{l=1}^{N_t} U\left(z_j, t_l\right) e^{-i\left(k z_j - \omega t_l\right)}, \tag{12}$$

where k is the axial wavenumber and $\omega = 2\pi f$ is angular frequency. The dispersion image is given by the magnitude spectrum

$$D\left(k, \omega\right) = \left|\tilde{U}\left(k, \omega\right)\right|, \tag{13}$$

in which guided-wave modes appear as ridges tracing their dispersion curves.

The accuracy of the reconstructed spectrum is controlled by both temporal and spatial acquisition. The frequency resolution is determined by the total recording duration ($\Delta f = 1/T$), while the wavenumber resolution depends on the aperture length, with longer apertures producing narrower lobes and enabling the separation of closely spaced modes. According to the Nyquist criterion, the maximum recoverable frequency and wavenumber are $f_{\max} = 1/\left(2\Delta t\right)$ and $k_{\max} = \pi/\Delta z$. Exceeding these limits introduces aliasing, where higher-frequency or higher-wavenumber content folds back into the passband. Furthermore, because both the temporal and spatial windows are finite, tapering functions (e.g., Hanning or Kaiser) are applied to mitigate sidelobes prior to transformation.

Although FEM-generated data are inherently noise-free, the use of two-dimensional Fourier analysis ensures consistency with experimental practice, where measurement noise and incomplete aperture coverage are unavoidable. When appropriate sampling criteria are satisfied, the extracted dispersion spectra provide an accurate representation of guided-wave propagation and serve as a direct bridge between numerical modeling and experimental measurement.

3. RESULTS AND DISCUSSIONS

Fig. 1 illustrates the FE model of the isotropic steel pipe simulated in COMSOL Multiphysics. The pipe was modeled as steel with density $\rho = 7850\,\mathrm{kg/m^3}$, Young's modulus $E = 210\,\mathrm{GPa}$, Poisson's ratio $\nu = 0.27$, and extended over a length of $L = 400\,\mathrm{mm}$. The inner and outer radii are chosen as $a = 50\,\mathrm{mm}$ and $b = 60\,\mathrm{mm}$, respectively. Perfectly matched layers (PMLs) were attached at both pipe ends to suppress spurious reflections. Excitation was applied using a circumferential ring transducer bonded to the pipe's outer surface. A broadband input was generated by superposing two Ricker wavelets centered at 1 MHz and 0.6 MHz. This combined excitation was applied at an effective incident angle of 45° relative to the pipe axis to enhance coupling into multiple longitudinal modes while minimizing torsional and flexural components. The computational regions were meshed with quadratic hexahedral elements using a swept scheme along the axial direction.

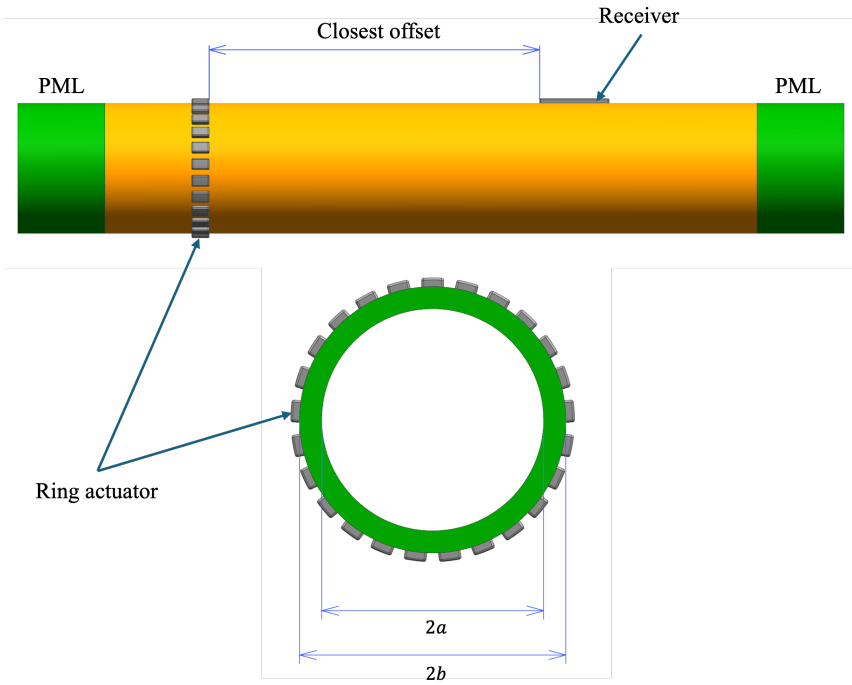

Fig. 1. Finite element model of the steel pipe with PML, ring actuator, and linear receiver array

To reproduce experimental acquisition, a linear receiver array was positioned along the pipe wall, beginning at a closest offset of $z_{\min} = 150\,\mathrm{mm}$ from the source. The array consisted of 60 receiver elements with uniform spacing (pitch $\Delta z = 1\,\mathrm{mm}$), yielding an effective aperture of $A_z = 59\,\mathrm{mm}$. Each receiver recorded the radial displacement response over the simulation window, and stacking these signals produced a two-dimensional time–space dataset, directly analogous to experimental multichannel measurements. This dataset serves as the foundation for dispersion spectrum reconstruction via two-dimensional Fourier analysis.

Representative time-domain responses recorded at the receiver array are shown in Fig. 2. The signals clearly consist of a superposition of multiple guided modes, leading to waveforms that deviate from the shape of the original Ricker pulse. The earliest arrival retains some similarity to the excitation, but subsequent oscillations arise from the dispersive propagation of higher-order modes. Importantly, no spurious trailing arrivals are observed, confirming the effectiveness of the PML boundaries in suppressing end reflections. The presence of multiple dispersive components indicates that the excitation couples into several dispersion branches

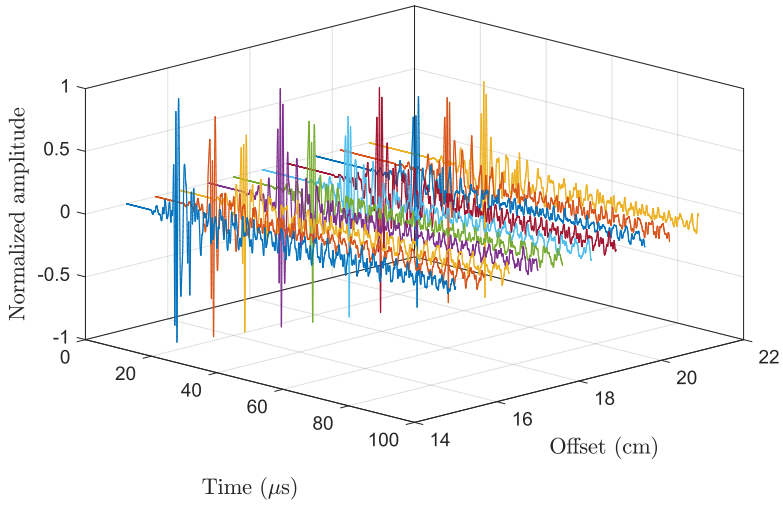

Fig. 2. Time-domain signals recorded at multi-element receiver

rather than a single mode. Collectively, these observations validate both the numerical implementation and the physical fidelity of the finite element model in reproducing guided wave propagation.

The reconstructed dispersion spectra obtained by applying a two-dimensional Fourier transform to the multichannel dataset are presented in Fig. 3, overlaid with theoretical dispersion solutions (provided in Appendix A). The comparison reveals excellent agreement between the FEM–acquisition framework and analytical predictions. Several longitudinal modes are clearly resolved, with the fundamental branches such as $L\,(0,1)$ and $L\,(0,2)$ dominating the spectra. These modes appear as strong, continuous ridges, consistent with their efficient coupling to the excitation and relatively low attenuation in the investigated frequency range.

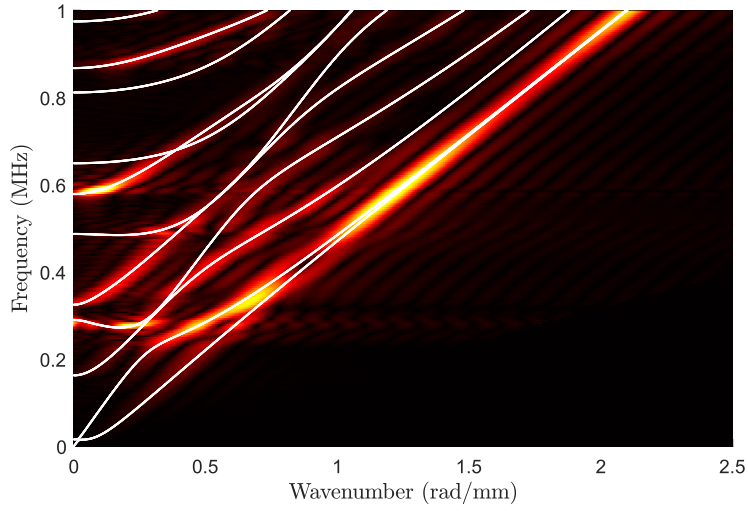

Fig. 3. Dispersion spectra reconstructed from 2D Fourier transform, overlaid with theoretical dispersion curves (white lines)

Higher-order longitudinal branches are less prominent, with some either absent or only partially visible. This selectivity can be attributed to the frequency-dependent coupling between the source spectrum and the modal displacement fields. In particular, the excitation bandwidth of the Ricker wavelet overlaps strongly with the lower-order modes but provides insufficient

energy to efficiently excite higher-order modes. Where partial recovery occurs, the ridges are confined to limited frequency ranges, fading once the excitation spectrum no longer coincides with the modal characteristics.

This behavior underscores a fundamental property of guided wave inspections: the observable dispersion image is not an exhaustive catalogue of all possible wave modes but rather a filtered representation shaped by excitation bandwidth, array aperture, and coupling efficiency. In practice, this selectivity is advantageous, since the most robust and easily excited modes are also the most useful for long-range inspection and defect detection.

The high fidelity of the reconstructed dispersion images validates the FEM–acquisition framework as a reliable bridge between numerical simulation and experimental measurement. By replicating realistic acquisition—including phased-array excitation and multichannel data recording—this approach produces datasets that are directly compatible with advanced post-processing and imaging algorithms.

From an application standpoint, the selective recovery of dominant modes highlights the importance of careful transducer design and frequency selection. For example, lower-order longitudinal modes such as $L(0,1)$ offer superior propagation distance and strong excitation efficiency, making them ideal for corrosion and wall-thickness monitoring. In contrast, partial excitation of higher-order branches can be advantageous when greater sensitivity is needed for detecting localized defects or geometric irregularities in the pipe wall, such as welds, thickness transitions, or small surface flaws.

Overall, the results demonstrate that the FEM–acquisition framework not only reproduces dispersion phenomena with high accuracy but also provides meaningful insights into mode selection, excitation efficiency, and signal interpretability—factors that are critical for optimizing pipeline inspection strategies.

4. CONCLUSIONS

This work presented a FE framework that replicates multichannel acquisition of guided waves in pipes. By combining phased-array excitation with distributed receivers, the approach produces time–space datasets from which dispersion spectra can be reconstructed using two-dimensional Fourier analysis. The extracted spectra showed excellent agreement with theoretical dispersion solutions, validating both the numerical implementation and the physical fidelity of the model. Importantly, the results demonstrated the selective recovery of dominant longitudinal modes such as $L(0,1)$ and $L(0,2)$, while higher-order branches were only partially captured, reflecting the frequency-dependent nature of excitation and coupling. Overall, the framework bridges conventional FEM modeling with experimental acquisition practice, offering realistic datasets for studying guided wave dispersion and supporting the development of inspection and signal-processing strategies. Future extensions may consider multilayered anisotropic pipes and defect scattering, thereby broadening the framework's applicability to practical nondestructive evaluation scenarios.

DECLARATION OF COMPETING INTEREST

The authors declare that they have no known competing financial interests or personal relationships that could have appeared to influence the work reported in this paper.

CREDIT AUTHOR STATEMENT

Ductho Le: *Conceptualization, Methodology, Investigation, Data curation, Formal analysis, Writing – original draft*. Hoang Ngoc Quy: *Methodology, Investigation, Validation, Writing – review & editing*. Haidang Phan: *Investigation, Resources, Visualization, Writing – review & editing*. Hoai Nguyen: *Conceptualization, Supervision, Project administration, Funding acquisition, Writing – review & editing*.

ACKNOWLEDGEMENT

This research is funded by Vietnam Academy of Science and Technology under grant number KHCBVL.04/23-24.

REFERENCES

Adamou, A. T. I., & Craster, R. V. (2004). Spectral methods for modelling guided waves in elastic media. *The Journal of the Acoustical Society of America*, *116*, 1524–1535. https://doi.org/10.1121/1.1777871

Chree, C. (1889). The equations of an isotropic elastic solid in polar and cylindrical coordinates. Their solution and application. *Transactions of the Cambridge Philosophical Society*, *14*, 251–369.

Cong, M., Wu, X., & Liu, R. (2017). Dispersion analysis of guided waves in the finned tube using the semi-analytical finite element method. *Journal of Sound and Vibration*, *401*, 114–126. https://doi.org/10.1016/j.jsv.2017.04.037

Cooper, R. M., & Naghdi, P. M. (1957). Propagation of nonaxially symmetric waves in elastic cylindrical shells. *The Journal of the Acoustical Society of America*, *29*, 1365–1373. https://doi.org/10.1121/1.1908812

Demma, A., Cawley, P., Lowe, M., & Pavlakovic, B. (2005). The effect of bends on the propagation of guided waves in pipes. *Journal of Pressure Vessel Technology*, *127*(3), 328–335. https://doi.org/10.1115/1.1990211

Gazis, D. C. (1959). Three-dimensional investigation of the propagation of waves in hollow circular cylinders. I. Analytical foundation. *The Journal of the Acoustical Society of America*, *31*(5), 568–573. https://doi.org/10.1121/1.1907753

Ghosh, J. (1923). Longitudinal vibrations of a hollow cylinder. *Bulletin of the Calcutta Mathematical Society*, *14*, 31–40.

Hayashi, T., Kawashima, K., Sun, Z., & Rose, J. L. (2003). Analysis of flexural mode focusing by a semianalytical finite element method. *The Journal of the Acoustical Society of America*, *113*, 1241–1248. https://doi.org/10.1121/1.1543931

Holmes, C., Drinkwater, B. W., & Wilcox, P. D. (2005). Post-processing of the full matrix of ultrasonic transmit–receive array data for non-destructive evaluation. *NDT & E International*, *38*(8), 701–711. https://doi.org/10.1016/j.ndteint.2005.04.002

Holmes, C., Drinkwater, B. W., & Wilcox, P. D. (2008). Advanced post-processing for scanned ultrasonic arrays: Application to defect detection and classification in non-destructive evaluation. *Ultrasonics*, *48*(6–7), 636–642. https://doi.org/10.1016/j.ultras.2008.07.019

Huthwaite, P., Ribichini, R., Cawley, P., & Lowe, M. J. S. (2013). Mode selection for corrosion detection in pipes and vessels via guided wave tomography. *IEEE Transactions on Ultrasonics, Ferroelectrics, and Frequency Control*, *60*(6), 1165–1177. https://doi.org/10.1109/tuffc.2013.2679

Jie, G., Yan, L., Mingfang, Z., Mingkun, L., Hongye, L., Bin, W., & Cunfu, H. (2021). Analysis of longitudinal guided wave propagation in the functionally graded hollow cylinder using state-vector formalism and legendre polynomial hybrid approach. *Journal of Nondestructive Evaluation*, *40*(1). https://doi.org/10.1007/s10921-021-00764-y

Kiefer, D. A. (2024). GEW dispersion script. https://doi.org/10.5281/ZENODO.7010603

Le, D., Tran, H.-N., Quy, H. N., & Phan, H. (2025). Guided wave propagation and scattering in pipes with axisymmetric defects under reciprocity considerations. *European Journal of Mechanics - A/Solids*, *111*. https://doi.org/10.1016/j.euromechsol.2025.105584

Le, D., Van Hung, N., Phan, H., Nguyen, Y., Van Quyen, T., & Le, Q. H. (2023). Analysis of longitudinal guided wave modes in pipe-like structures. *Computational Intelligence Methods for Green Technology and Sustainable Development*, 647–655. https://doi.org/10.1007/978-3-031-19694-2_57

Le, D., Phan, H., Nguyen, H., Sacchi, M. D., & Le, L. H. (2025). Guided waves in anisotropic and viscoelastic stratified plates: Application to bone quantitative ultrasound. *Computers & Structures*, *315*, 107820. https://doi.org/10.1016/j.compstruc.2025.107820

Lowe, P. S., Sanderson, R., Pedram, S. K., Boulgouris, N. V., & Mudge, P. (2015). Inspection of pipelines using the first longitudinal guided wave mode. *Physics Procedia*, *70*, 338–342. https://doi.org/10.1016/j.phpro.2015.08.079

Maess, M., Herrmann, J., & Gaul, L. (2007). Finite element analysis of guided waves in fluid-filled corrugated pipes. *The Journal of the Acoustical Society of America*, *121*(3), 1313–1323. https://doi.org/10.1121/1.2436711

Maruyama, T., Matsuo, T., & Nakahata, K. (2025). Numerical study on guided-wave reflection and transmission at water pipe joint using hybrid finite element method. *Computational Mechanics*, *75*(1), 285–300. https://doi.org/10.1007/s00466-024-02505-0

Nasedkina, A. A., Alexiev, A., & Malachowski, J. (2016). Numerical simulation of ultrasonic torsional guided wave propagation for pipes with defects. *Advanced Materials*, 475–488. https://doi.org/10.1007/978-3-319-26324-3_33

Pochhammer, L. (1876). Ueber die Fortpflanzungsgeschwindigkeiten kleiner Schwingungen in einem unbegrenzten isotropen Kreiscylinder. *Journal für die reine und angewandte Mathematik*, *1876*(81), 324–336. https://doi.org/10.1515/crll.1876.81.324

Predoi, M. V. (2014). Guided waves dispersion equations for orthotropic multilayered pipes solved using standard finite elements code. *Ultrasonics*, *54*(7), 1825–1831. https://doi.org/10.1016/j.ultras.2014.01.019

Qu, J., & Jacobs, L. (2003). Cylindrical waveguides and their applications in ultrasonic evaluation. *Ultrasonic Nondestructive Evaluation: Engineering and Biological Material Characterization*, 311–362. https://doi.org/10.1201/9780203501962.ch5

Rose, J. L. (2014). *Ultrasonic guided waves in solid media* (1st). Cambridge University Press. https://doi.org/10.1017/CBO9781107273610

Sarwar, U., Mokhtar, A. A., Muhammad, M., Wassan, R. K., Soomro, A. A., Wassan, M. A., & Kaka, S. (2024). Enhancing pipeline integrity: A comprehensive review of deep learning-enabled finite element analysis for stress corrosion cracking prediction. *Engineering Applications of Computational Fluid Mechanics*, *18*(1). https://doi.org/10.1080/19942060.2024.2302906

Sorohan, Ş., Constantin, N., Găvan, M., & Anghel, V. (2011). Extraction of dispersion curves for waves propagating in free complex waveguides by standard finite element codes. *Ultrasonics*, *51*(4), 503–515. https://doi.org/10.1016/j.ultras.2010.12.003

Sun, Z., Zhang, L., & Rose, J. L. (2005). Flexural torsional guided wave mechanics and focusing in pipe. *Journal of Pressure Vessel Technology*, *127*, 471–478. https://doi.org/10.1115/1.2065587

Zang, X., Xu, Z.-D., Lu, H., Zhu, C., & Zhang, Z. (2023). Ultrasonic guided wave techniques and applications in pipeline defect detection: A review. *International Journal of Pressure Vessels and Piping*, *206*. https://doi.org/10.1016/j.ijpvp.2023.105033

Zhang, X., Li, Z., Wang, X., & Yu, J. (2021). The fractional Kelvin-Voigt model for circumferential guided waves in a viscoelastic FGM hollow cylinder. *Applied Mathematical Modelling*, *89*, 299–313. https://doi.org/10.1016/j.apm.2020.06.077

APPENDIX A.

The theoretical dispersion curves are obtained by solving the characteristic equation of an isotropic hollow cylinder, as expressed in Eq. (A.1). The detailed derivation of this equation can be found in Le et al. (2023).

$$\det \begin{bmatrix} \mathbf{X}^Z(a) & \mathbf{X}^W(a) \\ \mathbf{X}^Z(b) & \mathbf{X}^W(b) \end{bmatrix} = 0, \tag{A.1}$$

where $\mathbf{X}^{\mathcal{B}}\left(\mathcal{B}=Z,W\right)$ is a 2×2 matrix containing Bessel functions of type $\mathcal{B}$. The components of $\mathbf{X}^{\mathcal{B}}$ are defined as follows

$$\begin{aligned}
\mathbf{X}_{11}^{\mathcal{B}}\left(r\right) &= -\lambda\left(p_1^2+k^2\right)\mathcal{B}_0\left(pr\right)+2\mu\mathcal{B}_0''\left(pr\right),\\
\mathbf{X}_{12}^{\mathcal{B}}\left(r\right) &= 2ik\mu\mathcal{B}_1'\left(qr\right),\\
\mathbf{X}_{21}^{\mathcal{B}}\left(r\right) &= 2ik\mu\mathcal{B}_0'\left(pr\right),\\
\mathbf{X}_{22}^{\mathcal{B}}\left(r\right) &= \left(q_1^2-k^2\right)\mathcal{B}_1\left(qr\right).
\end{aligned} \tag{A.2}$$

The definitions of the parameters in Eq. (A.2) can be found in Le et al. (2023).